AGU PUBLICATIONS

JGR

Journal of Geophysical Research: Oceans

RESEARCH ARTICLE

10.1002/2015JC011268

Key Points:
- Nonlinear energy transfers to and from infragravity frequencies depend on beach slope
- Infragravity frequencies interact with the spectral peak during dissipation on a steep beach
- On a gentle beach infragravity-infragravity interactions dominate during dissipation

Correspondence to:
A. T. M. de Bakker,
a.t.m.debakker@uu.nl

Citation:
de Bakker, A. T. M., M. F. S. Tissier, and B. G. Ruessink (2016), Beach steepness effects on nonlinear infragravity-wave interactions: A numerical study, *J. Geophys. Res. Oceans*, *121*, 554–570, doi:10.1002/2015JC011268.

Received 24 AUG 2015
Accepted 14 DEC 2015
Accepted article online 18 DEC 2015
Published online 14 JAN 2016

Beach steepness effects on nonlinear infragravity-wave interactions: A numerical study

A. T. M. de Bakker[1], M. F. S. Tissier[2], and B. G. Ruessink[1]

[1]Faculty of Geosciences, Department of Physical Geography, Utrecht University, Utrecht, Netherlands, [2]Faculty of Civil Engineering and Geosciences, Environmental Fluid Mechanics Section, Delft University of Technology, Delft, Netherlands

Abstract The numerical model SWASH is used to investigate nonlinear energy transfers between waves for a diverse set of beach profiles and wave conditions, with a specific focus on infragravity waves. We use bispectral analysis to study the nonlinear triad interactions, and estimate energy transfers to determine energy flows within the spectra. The energy transfers are divided into four types of triad interactions, with triads including either one, two or three infragravity-frequency components, and triad interactions solely between sea-swell wave frequencies. The SWASH model is validated with a high-resolution laboratory data set on a gently sloping beach, which shows that SWASH is capable of modeling the detailed nonlinear interactions. From the simulations, we observe that especially the beach slope affects nonlinear infragravity-wave interactions. On a low-sloping beach, infragravity-wave energy dominates the water motion close to shore. Here infragravity-infragravity interactions dominate and generate higher harmonics that lead to the steepening of the infragravity wave and eventually breaking, causing large infragravity energy dissipation. On the contrary, on a steep-sloping beach, sea-swell wave energy dominates the water motion everywhere. Here infragravity frequencies interact with the spectral peak and spread energy to a wide range of higher frequencies, with relatively less infragravity energy dissipation. Although both beach types have different nonlinear interaction patterns during infragravity-wave dissipation, the amount of infragravity-wave reflection can be estimated by a single parameter, the normalized bed slope.

1. Introduction

During shoreward propagation of ocean waves, energy is transferred away from the spectral peak(s) f_p in the sea-swell frequency range (0.05–0.5 Hz). These energy transfers take place between three phase-coupled frequencies and are called nonlinear triad interactions. Sum interactions ($f_1+f_2=f_3$) transfer energy from the spectral peak to multiples of the spectral peak, often called higher harmonics (where $f_1 \approx f_2 \approx f_p$ and $f_3 \approx 2f_p$). The development of higher harmonics is linked to the skewed shape of sea-swell waves during shoaling, and the asymmetric, sawtooth like shape during breaking, very close to shore [e.g., *Elgar and Guza*, 1985]. Simultaneous with the sea-swell wave shape transformation, energy is transferred to lower, infragravity frequencies (0.005–0.05 Hz) by difference interactions ($f_1-f_2=f_3$), forming bound long waves [e.g., *Elgar and Guza*, 1985]. In the surf zone, the infragravity waves are released and propagate to the shore as free waves, where they (partly) reflect [e.g., *Longuet-Higgins and Stewart*, 1962; *Herbers et al.*, 1995b; *Ruessink*, 1998]. Infragravity waves may dominate the water motion close to shore, where they generally reach their maximum amplitude and where sea-swell wave energy has by then largely dissipated [e.g., *Guza and Thornton*, 1982; *Russell*, 1993; *Sénéchal et al.*, 2011]. Consequently, infragravity waves can be important for the erosion of beaches and dunes, especially during storms [e.g., *Russell*, 1993; *Van Thiel de Vries et al.*, 2007].

Recently, several studies have shown that shoreward-propagating infragravity waves can loose a considerable part of their energy near the shoreline [e.g., *Ruessink*, 1998; *Sheremet et al.*, 2002; *Battjes* et al., 2004; *Thomson et al.*, 2006; *Henderson et al.*, 2006; *Van Dongeren et al.*, 2007; *Sénéchal et al.*, 2011; *Ruju et al.*, 2012; *Guedes et al.*, 2013; *De Bakker et al.*, 2014, 2015]. The causes of this infragravity-wave energy dissipation have been the subject of debate during the last years. Contrary to coral reef sites where friction can be very important [*Pomeroy et al.*, 2012; *Van Dongeren et al.*, 2013], on sandy beaches bottom friction is considered to be a secondary dissipation mechanism [e.g., *Henderson et al.*, 2006; *Van Dongeren et al.*, 2007; *Lin and Hwung*, 2012; *Van Dongeren et al.*, 2013; *De Bakker et al.*, 2014]. Instead, two other mechanisms have been

proposed to explain the loss of infragravity-wave energy, both related to nonlinear triad interactions. One is the transfer of energy from infragravity-wave frequencies back to the spectral peak and/or its higher harmonics [*Henderson et al*., 2006; *Thomson et al*., 2006; *Ruju et al*., 2012; *Guedes et al*., 2013]. The other mechanism is the development of infragravity-infragravity interactions, which lead to the development of infragravity (higher) harmonics that allow for the steepening of the infragravity wave and eventually its breaking [*Battjes et al*., 2004; *Van Dongeren et al*., 2007; *Lin and Hwung*, 2012; *Ruju et al*., 2012; *De Bakker et al*., 2014]. The observations of two different types of nonlinear interactions during infragravity-wave dissipation is potentially related to the different site characteristics. *Henderson et al*. [2006] and *Thomson et al*. [2006] observed energy transfers from infragravity-wave frequencies back to the spectral peak and/or its higher harmonics on rather mild (1:50) to steep (1:15) sloping beaches respectively, when infragravity-wave energy was small compared to that in the sea-swell band. *Guedes et al*. [2013] observed that this transfer accounted for a small part of the total infragravity-wave energy loss only on their gently (1:70) sloping field site. Laboratory and field observations on more gently sloping beaches (1:35–1:80), where infragravity waves can dominate over sea-swell waves, identify breaking as dominant dissipation mechanism [*Battjes et al*., 2004; *Van Dongeren et al*., 2007; *Lin and Hwung*, 2012; *De Bakker et al*., 2014]. *Ruju et al*. [2012] used numerical modeling on 1:20–1:30 sloping beaches to show that both mechanisms account partly for the infragravity-wave energy loss. In the outer part of the sea-swell surf zone, where sea-swell wave energy is still considerable, energy is transferred back to sea-swell peaks, whereas in shallower water, where sea-swell wave energy has largely dissipated, the dominant interactions are infragravity-infragravity interactions.

Norheim et al. [1998] investigated the effect of the beach profile on nonlinear interactions in general, through a field data-model comparison, and concluded that on a gentle slope sea-swell sub and higher harmonics grow more than on a steeper slope. In addition, *Thomson et al*. [2006] observed a dependence of energy transfers on the beach shape; although the total surf zone width was not seen to change between a convex (low tide) and concave (high tide) profile, energy transfers including infragravity frequencies were enhanced over the convex profile. Most likely, this is caused by the larger horizontal extent of the region with shallow ($<$ 1 m) water depth, where triad interactions are closer to resonance [*Freilich and Guza*, 1984; *Herbers et al*., 1995a]. *Norheim et al*. [1998] also analyzed nonbreaking waves progressing over a bar, and observed an energy reversal on the downward slope after the bar, with energy going from high to low sea-swell frequencies. Interestingly, infragravity waves were not affected and continued to receive energy from the spectral peak. Also the effect of offshore wave conditions on nonlinear interactions has been studied. Previous studies have shown that high energetic conditions show considerably stronger nonlinear interactions than low energetic conditions [*Herbers et al*., 1994; *Norheim et al*., 1998; *De Bakker et al*., 2015]. In addition, the shape of the energy spectrum was seen to influence the strength of the nonlinear coupling and the number of frequencies involved; with narrow-banded spectra interactions were stronger and limited to a smaller number of frequencies, compared to broad-banded spectra [e.g., *Elgar and Guza*, 1985; *Norheim et al*., 1998; *De Bakker et al*., 2015]. A large directional spread was observed to decrease nonlinear difference interactions considerably [*Hasselmann et al*., 1963; *Herbers et al*., 1994; *Herbers and Burton*, 1997]. For a 30° directional spread, *Herbers et al*. [1994] observed the growth of the forced infragravity waves to be reduced by an order of magnitude compared to the case without directional spread.

We hypothesize that beach characteristics and offshore wave conditions influence not only the strength but also the type of nonlinear infragravity-wave transfers observed during infragravity-wave dissipation. We aim to shed light on the relative importance of the two different nonlinear interaction patterns observed in previous studies (energy transfer back to sea-swell frequencies and infragravity-infragravity interaction) during infragravity-wave dissipation. To this end, we here study energy transfers including infragravity frequencies by analyzing energy transfer patterns for different types of idealized one-dimensional beaches using the numerical model SWASH [*Zijlema et al*., 2011]. In section 2, SWASH is described and validated with a high-resolution, small-scale laboratory data set obtained on a gently (1:80) sloping beach [*De Bakker et al*., 2015]. Section 3 compares these results with numerical simulations on a mild (1:50) and steep (1:20) sloping profile, to study the effect of beach steepness on nonlinear energy transfers. In addition, a convex and a concave configuration are introduced to address the effects of the beach shape, rather than the steepness alone, on the energy transfer patterns. Furthermore, offshore wave conditions are varied over a number of beach profiles to test the robustness of the results. In section 4, modeled trends in infragravity-wave reflection are discussed. Conclusions are given in section 5.

2. Methods

2.1. Numerical Model

We use the numerical model SWASH to simulate the transformation of nearshore wavefields over variable profiles. SWASH is a nonhydrostatic model based on the nonlinear shallow water equations [*Zijlema et al.*, 2011] and has shown to accurately capture the nearshore processes of breaking [*Smit et al.*, 2013], infragravity wave dynamics [*Rijnsdorp et al.*, 2012, 2015], run-up oscillations [*Ruju et al.*, 2014] and nonlinear wave dynamics [*Smit et al.*, 2014].

Because the SWASH model will be used here to study wave propagation in a cross-shore/one-dimensional setting, the governing equations can be written as

$$\frac{\partial \eta}{\partial t}+\frac{\partial}{\partial x}\int_{-d}^{\eta} u dz=0, \tag{1}$$

$$\frac{\partial u}{\partial t}+\frac{\partial uu}{\partial x}+\frac{\partial wu}{\partial z}+\frac{\partial wu}{\partial z}=-\frac{1}{\rho}\frac{\partial(p_h+p_{nh})}{\partial x}+\frac{\partial \tau_{xz}}{\partial z}+\frac{\partial \tau_{xx}}{\partial x}, \tag{2}$$

$$\frac{\partial w}{\partial t}+\frac{\partial uw}{\partial x}+\frac{\partial ww}{\partial z}=-\frac{1}{\rho}\frac{\partial p_{nh}}{\partial z}+\frac{\partial \tau_{zz}}{\partial z}+\frac{\partial \tau_{zx}}{\partial x}, \tag{3}$$

$$\frac{\partial u}{\partial x}+\frac{\partial w}{\partial z}=0, \tag{4}$$

with x and z the horizontal and vertical coordinate, respectively, with z positive above the still water level ($z=-d$ at the bottom). The free surface elevation η is relative to the still water level, t is time, $u(x,z,t)$ and $w(x,z,t)$ are the horizontal and vertical velocities, respectively, and ρ is the density. $p_h=\rho g(\eta-z)$ is the hydrostatic pressure and p_{nh} the nonhydrostatic pressure contribution. The turbulent stresses τ are obtained from a turbulent viscosity approximation (e.g., $\tau_{xz}=\nu\frac{\partial u}{\partial z}$, where ν is the horizontal eddy viscosity) using a standard $\kappa-\epsilon$ model.

A bottom stress is included at the bottom boundary using a quadratic friction law,

$$\tau_{b,x}=c_f\frac{U|U|}{h}, \tag{5}$$

with $h=\eta+d$ the total water depth, U the depth-averaged velocity and c_f a dimensionless friction coefficient. In the present study, the dimensionless friction coefficient is calculated as [*Zijlema et al.*, 2011],

$$c_f=\frac{n^2 g}{h^{1/3}}, \tag{6}$$

with Manning's roughness coefficient n. For a full model description, we refer to *Zijlema et al.* [2011].

The model's vertical resolution is set to 6 layers as suggested by *Smit et al.* [2014], who show that the frequency dispersion is then accurately solved up to high kd values, where k is the wavenumber (relative error $<0.1\%$ for $kd<40$). Wave breaking is handled using the approach introduced in *Smit et al.* [2013]. Wave breaking is initiated when the vertical velocity of the free surface $\partial_t\eta$ exceeds a threshold ratio (α_1) of the shallow water wave celerity $\sqrt{gh}$. The pressure at the wave front is then forced to be hydrostatic ($p_{nh}=0$) allowing the front to develop into a discontinuity where energy is dissipated in analogy to a hydraulic jump. Wave breaking is terminated when $\partial_t\eta/\sqrt{gh}$ becomes less than a second threshold $\alpha_2<\alpha_1$. For a vertical resolution of 6 layers, $\alpha_1=1$ and $\alpha_2=0.3$ are recommended [*Smit et al.*, 2014] and used here. The model's output comprises time series of η and U at a number of predefined cross-shore positions.

2.2. Model Set-Up and Validation

The SWASH model was validated with the high-resolution GLOBEX laboratory data set, obtained in the Schelde flume (The Netherlands) in 2012. The flume is 110 m long, 1 m wide and 1.2 m high and has a piston-type wave maker equipped with an Active Reflection Compensation (ARC). A fixed, low-sloping (1:80) concrete beach was constructed over almost the entire length of the flume, except for the first 16.6 m that were horizontal and where the mean water level was 0.85 m (Figure 1). This corresponds to a depth of 17 m in prototype, leading to a depth scale factor of 0.05. Here, three irregular-wave cases are studied: an

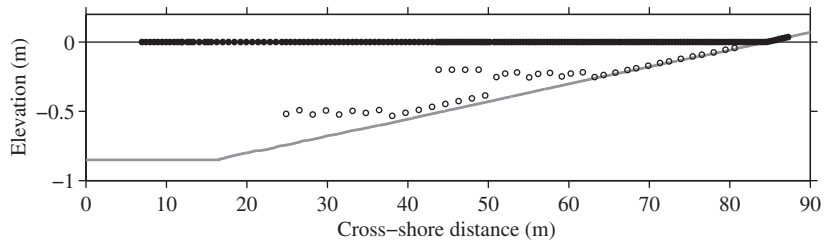

Figure 1. Elevation z versus cross-shore distance x in the Scheldegoot during the GLOBEX project. Here $x = 0$ is the location of the wavemaker at rest, and $z = 0$ corresponds to the still water level. At $x = 84.6$ m the still water level intersected with the bed. The 190 dots are the positions of the wave gauges, the 43 circles are the positions and heights above the bed of the electromagnetic current meters.

intermediate energy sea-wave condition *A*1, a high-energy sea-wave condition *A*2, and a narrow-banded swell condition *A*3. All wave-paddle steering signals were based on a JONSWAP spectrum with a peak enhancement factor γ as specified in Table 1. Water level data and cross-shore flow-velocity data were obtained at 190 and 43 positions, respectively (Figure 1), both sampled at 128 Hz. Total record length excluding the spin-up at the start was 69 min. See *Ruessink et al*. [2013] and *De Bakker et al*. [2015] for further details and initial data processing.

To accurately resolve the wave motion, a spatial resolution of 0.02 m was chosen, which is about 1/50 of the sea-swell spectral peak wave length in the inner surf zone. A time step of 0.002 seconds was used (corresponding to a Courant number of roughly 0.3). The bed friction coefficient, c_f, was calculated with $n = 0.015$ s/m$^{1/3}$, a typical value for unfinished concrete [*Chow*, 1959]. To account for all forms of unresolved vertical mixing, and to improve numerical stability, a background viscosity of 3 x 10^{-4} m^2/s was added as a fixed value. The model was forced with Fourier transforms of the free surface signal of the sea-swell wave frequencies up to $f = 2.5$ Hz, at the mean position of the wavemaker. The initial time series at the wavemaker were first resampled to 10 Hz. A second-order correction, based on weakly nonlinear wave theory, was added to resolve the incident bound infragravity waves at the offshore generating boundary [*Rijnsdorp et al*., 2012]. A weakly reflective boundary was used at the wavemaker to avoid rereflection at infragravity frequencies.

Comparisons between the modeled and measured sea-swell- wave heights are shown in Figures 2a–2c. The significant wave height for both the sea-swell (H_{SW}) and infragravity-wave (H_{IG}) range was calculated as four times the standard deviation of the sea-surface elevation of each frequency range. The separation frequencies f_{IG} of 0.37 Hz (*A*1, $f_p = 0.63$ Hz) and 0.26 Hz (*A*2 and *A*3, $f_p = 0.44$ Hz) were chosen because the variance density spectra of η at the wave gauge closest to the wave maker contained a minimum at these frequencies. For all three wave conditions, the onset of sea-swell wave breaking and their dissipation trend are seen to be captured very well (squared correlation coefficients for the sea-swell wave height $R_c^2 \geq 0.97$). However, small offsets are present well seaward of the surf zone ($x < 30$ m), where the model underestimates the sea-swell wave height slightly. The decrease in sea-swell wave heights in the shoaling zone is probably due to bed and side-wall friction, as visual observations during the experiment did not identify any breaking. Figures 2d–2f show infragravity-wave heights for incoming and outgoing infragravity-wave signals. The incoming and outgoing wave signals are separated with the *Guza et al*. [1984] time-domain approach, which uses colocated η and u sensors. We use a depth-averaged velocity value from the model output, and a specific point measurement for the laboratory data. To minimize any reflection-related noise, the incoming wave-signal is used for all following bispectral calculations. The infragravity-wave height growth and arrest are captured well, with only a slight underestimation by the model for condition *A*2 (Figure 2e). R_c^2-values for the incoming infragravity wave are all above 0.97. In both the data and the model, the outgoing infragravity-wave is seen to be substantially smaller than the incoming infragravity-wave, indicating strong energy dissipation. However, the model underestimates the outgoing infragravity-wave height noticeably within the sea-swell wave surf zone, indicating that the infragravity-wave dissipation was over predicted, leading to low R_c^2 values of 0.6 for case *A*1 and 0.39 for case *A*3 and only 0.04 for case *A*2. The total infragravity-wave signal is however not affected considerably by the rather poor predictive skill of the outgoing waves, and shows high R_c^2 values ≥ 0.95, for all three

Table 1. Test Conditions Irregular Wave Cases

Case	$H_s(m)$	$T_p(s)$	γ
*A*1	0.1	1.58	3.3
*A*2	0.2	2.25	3.3
*A*3	0.1	2.25	20

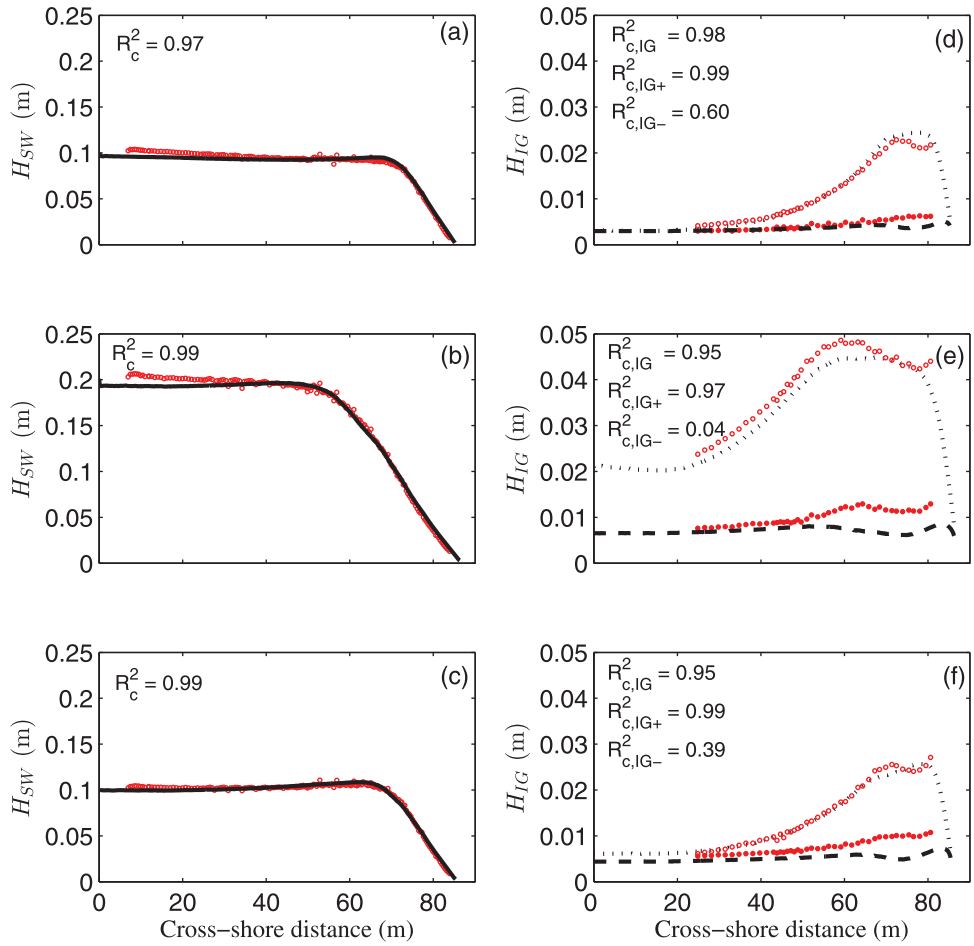

Figure 2. Observed (red dots) and modeled (black lines) significant wave height versus cross-shore distance x, for sea-swell waves H_{SW} (a) case $A1$, (b) case $A2$, and (c) case $A3$. Significant incoming (circles/dotted line) and outgoing (dots/dashed line) infragravity-wave heights H_{IG} calculated from separated signals at locations of the electromagnetic current meters (following *Guza et al.* [1984]) for (d) case $A1$, (e) case $A2$, and (f) case $A3$. R_c^2 is the squared correlation coefficient.

conditions. This overestimation of infragravity-wave dissipation was also observed in field-scale simulations using SWASH for a natural site [*Rijnsdorp et al.*, 2015]. Varying our friction coefficient affected the model predictions only slightly, and did therefore not result in more accurate predictions. Moreover, this suggests that bed friction is not the dominant source for the strong infragravity-wave dissipation. As the laboratory measurements can only give incoming wave signals up to $x = 80.6$ m ($h = 0.057$ m), where the most onshore colocated η - u sensors were positioned, the model allows us to visualize the large decrease in incoming infragravity-wave height shoreward of that point, up to the shoreline (here defined as the most onshore wet point in the model). A peculiar infragravity-wave height variation is observed in the surf zone; for example see case $A2$, where at $x = 60$ m the incoming infragravity wave height decreases, and subsequently increases at $x = 80$ m. This "wiggle" in both incoming and outgoing infragravity wave height present in the sea-swell surf zone (especially clear in the measurements) is more pronounced for low infragravity frequencies (not shown). It is most likely caused by relatively strong reflection at $f < 0.05$ Hz. Also, the *Guza et al.* [1984] $\eta^{\pm}$ separation method, based on linear wave theory, is expected to have limited reliability in these very shallow waters.

Figure 3 compares modeled and measured power spectra for wave condition $A3$ at three cross-shore locations. We choose to show case $A3$ as its clear peaks in the power and bispectra facilitate the interpretation, compared to the two cases with more broad-banded waves. The measured spectral evolution is closely followed by the model (R_c^2 of the base 10 logarithm of the power spectrum ≥ 0.98), only at very low infragravity frequencies ($f < 0.05$ Hz) a slight mismatch is present. In the shoaling zone the spectra have a clear peak at sea-swell frequencies, and a number of higher harmonics can be identified (Figure 3a). In the outer surf

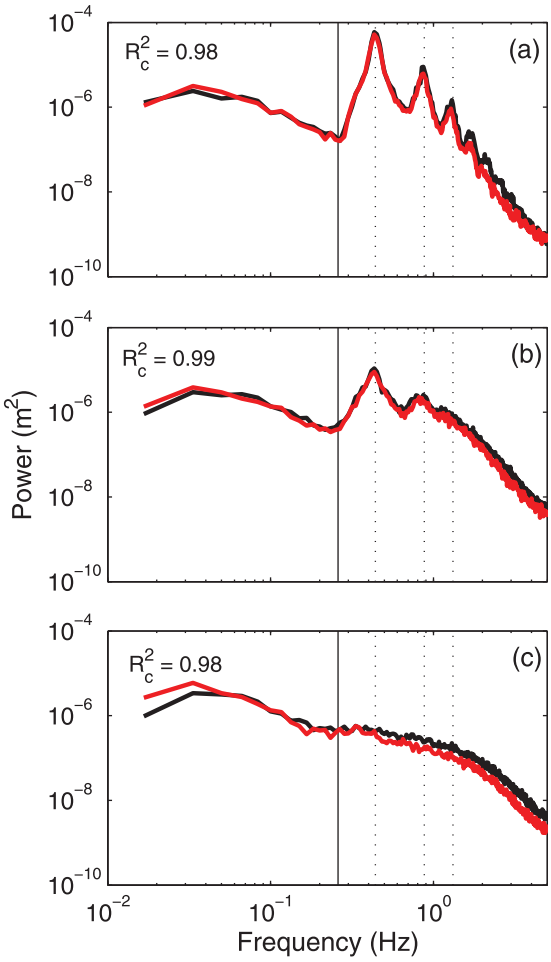

Figure 3. Modeled (black) and observed (red) power spectra for case *A*3, in the (a) shoaling ($x = 63.2$ m, $h = 0.26$ m), (b) outer surf ($x = 73.9$ m, $h = 0.13$ m), and (c) inner surf zone ($x = 80.6$ m, $h = 0.06$ m). The vertical solid line indicates the cutoff between infragravity and sea-swell wave frequencies. Vertical dashed lines indicate offshore power spectral peak ($f = 0.44$ Hz) and its first ($f = 0.88$ Hz) and second ($f = 1.32$ Hz) harmonic. R_c^2 is the squared correlation coefficient of the base 10 logarithm of the power.

zone (defined here as the first half of the sea-swell surf zone) the offshore spectral peak decreases, together with its higher harmonics (Figure 3b). Close to shore, the offshore spectral peak has completely dissipated, and infragravity energy dominates (Figure 3c). For cases *A*1 and *A*2 results are similar (not shown).

To investigate the nonlinear interactions within the wave field as it travels shoreward, bispectra were calculated following *Hasselmann et al.* [1963]. The bispectrum $B_{f1,f2}$ detects phase-coupling between frequency components in a triad. The normalized magnitude of the bispectrum, called the bicoherence $b^2_{f_1,f_2}$, provides a normalized measure of the strength of the coupling of the interacting wave components and is computed following *Collis et al.* [1998, equation (27)]. The normalized phase of the interacting components is called the biphase β_{f_1,f_2} and is calculated following *Kim and Powers* [1979]. Energy transfers to and from a frequency *f* can be calculated with the nonlinear source term S_{nl}, for more detail see Appendix A. Both observed and modeled data were divided into blocks of 15 min, averaging of the bispectral estimates over 15 frequencies resulted in a frequency resolution of 0.0167 Hz and 240 degrees of freedom. Bicoherence values larger than 0.1581 are statistically significant from 0 at the 95% confidence level, based on the approximation of *Kim and Powers* [1979]. Figure 4 shows the imaginary part of the bispectrum for the modeled and measured wave conditions at the same locations as above. The imaginary part of the bispectrum shows the relative energy transfers, to quantify the transfers, the bispectral values need to be multiplied with an interaction coefficient, see equation (A1). Positive (red) values at B_{f_1,f_2} indicate a transfer from f_1 and f_2 to f_3, the sum frequency. Negative (blue) values indicate a transfer from f_3 to f_1 and f_2. In the shoaling zone (Figures 4a and 4d), the model predictions and the measurements both show a positive interaction at $B(0.44, 0.44)$ where energy is transferred from the spectral peak to its higher harmonic at $f = 0.88$ Hz. Another positive, less strong interaction, is present at $B(0.88, 0.44)$ where energy is transferred from the spectral peak and its first harmonic to the second harmonic at $f = 1.32$ Hz. At the same time, negative interactions are present at $B(0.42, 0.04)$ with energy transfers from $f_3 = 0.46$ Hz to both $f_1 = 0.42$ Hz and $f_2 = 0.04$ Hz, and at $B(0.86, 0.04)$ with energy transfers from $f_3 = 0.90$ Hz to both $f_1 = 0.86$ Hz and $f_2 = 0.04$ Hz. These two interactions are responsible for the growth of the bound infragravity wave, while at the same time causing the energy around the spectral peak and its harmonics to shift to slightly lower frequencies, see also *De Bakker et al.* [2015]. In the outer surf zone (Figures 4b and 4e) energy transfers weaken (note the different color scale) and two other interactions become visible in both the data and the model. The negative peak at $\approx B(0.36, 0.07)$ is here clearly accompanied by a positive peak at $\approx B(0.45, 0.07)$ indicating that infragravity-wave components act as conduits in interactions that broaden the spectral peak. Furthermore, interactions between infragravity waves develop that transfer energy from $f \approx 0.07$ Hz to lower and higher infragravity frequencies; a negative interaction at $\approx B$ (0.035,0.035) transfers energy from $f \approx 0.07$ Hz to $f \approx 0.035$ Hz, creating an infragravity subharmonic, and a positive interaction at $\approx B$ (0.07,0.07) transfers

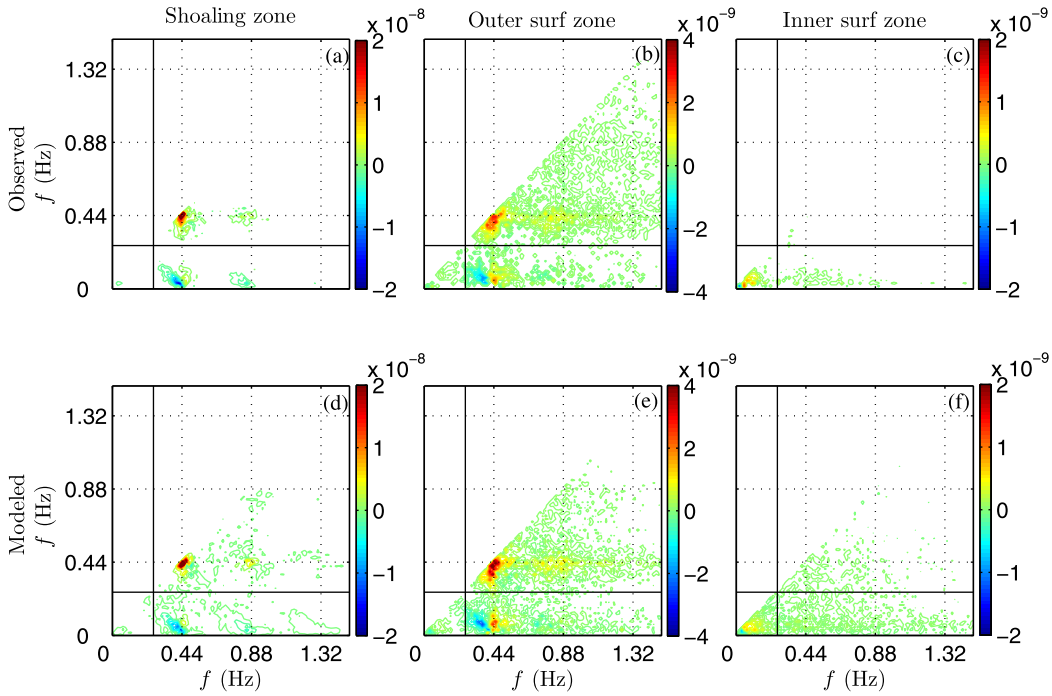

Figure 4. (top) Observed and (bottom) modeled imaginary part of the bispectrum of the incoming wave signal (η^+) over a 1:80 slope, at three cross-shore locations for case *A*3, for values where $b^2 > b^2_{95\%}$. (a, d) $x = 63.2$ m, $h = 0.26$ m, (b, e) $x = 73.9$ m, $h = 0.13$ m, (c, f) $x = 80.6$ m, $h = 0.06$ m. Black solid lines indicate the cutoff between infragravity and sea-swell wave frequencies, f_{IG}. Dashed lines indicate the spectral peak ($f = 0.44$ Hz) and its higher harmonics.

energy to $f \approx 0.15$ Hz, creating what may be called a higher harmonic of the infragravity waves. The infragravity-infragravity interactions are slightly overpredicted in the model. Close to the shoreline, only interactions between infragravity waves are significant (Figures 4c and 4f), which transfer energy predominantly to the higher infragravity frequencies.

Overall, the model shows trends and magnitudes very similar to the measurements, demonstrating SWASH is capable of modeling the detailed nonlinear interactions. The overestimation of the infragravity-infragravity interactions in very shallow water by the model may cause the underestimation in outgoing infragravity wave height in the inner surf zone (see Figures 2d–2f), and the reduced R^2.

3. Results

3.1. Uniform Slope

Figure 5 shows the modeled nonlinear energy transfers S_{nl} of case *A*3 plotted versus frequency and cross-shore position for each of the four bispectral zones. In the shoaling zone, dominant interactions are the ones solely between sea-swell wave components ($S_{nl,IV}$, Figure 5d). The spectral peak transfers energy to its higher harmonics up to the outer edge of the surf zone, defined as the maximum sea-swell significant wave height. From here onward the spectral peak looses energy strongly to its harmonics and to a whole range of higher frequencies. Triads including two sea-swell and one infragravity frequency are important in generating energy at infragravity frequencies and spreading energy around the spectral peaks (as seen in the bispectra) ($S_{nl,III}$, Figure 5c). In the surf zone, infragravity frequencies receive more energy through triad interactions with only one sea-swell frequency ($S_{nl,II}$, Figure 5b). Close to shore, when sea-swell energy has largely dissipated, triads with two or more infragravity frequencies become important, and energy cascades from low infragravity frequencies to high infragravity frequencies ($S_{nl,I}$, Figure 5a), and from there to what might be called a higher infragravity harmonic ($S_{nl,II}$, Figure 5b).

The laboratory set-up with the 1:80 slope is considered as the reference profile on which four new profiles are varied. To study the effect of the bed slope on the energy exchanges in the wave field, at 85% of the offshore wave energy ($x \approx 45$ m), the 1:80 slope is changed into a steep (1:20) and a mild (1:50) slope (Figure 6c).

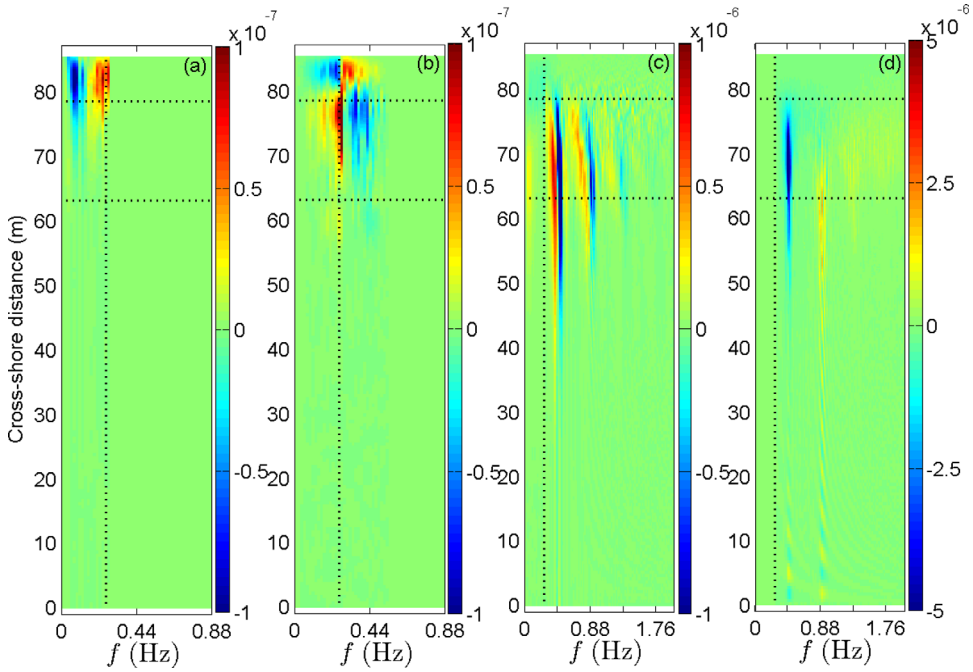

Figure 5. Nonlinear source term S_{nl} estimated from the modeled incoming wave signal of case *A*3 on a 1:80 slope, versus frequency *f* and cross-shore position *x*. With (a) infragravity frequencies only ($S_{nl,I}$), (b) two infragravity and one sea-swell frequency ($S_{nl,II}$), (c) two sea-swell and one infragravity frequency ($S_{nl,III}$), and (d) sea-swell frequencies only ($S_{nl,IV}$). The horizontal dashed lines indicate the locations of the maximum infragravity ($x = 78.3$ m) and sea-swell ($x = 63.0$ m) wave heights just before dissipation starts. The vertical dashed line indicates the cutoff between infragravity and sea-swell frequencies. Note the different *x*-axis and color scaling for Figures 5a and 5b versus Figures 5c and 5d.

Because *Thomson et al.* [2006] observed that also the beach shape, rather than steepness alone, influenced the strength of the energy transfers considerably, we also introduce a concave ($x^{4/3}$) and a convex ($x^{2/3}$) profile (Figure 6f). Figure 6a shows the modeled sea-swell wave heights for narrow-banded case *A*3 propagating over a steep 1:20 profile, a mild 1:50 profile, and a gentle 1:80 profile (the validation case). On the steep profile the sea-swell waves reach shallow water sooner, and have a relatively narrow surf zone compared to the milder sloping profiles. Figure 6b shows the incoming and outgoing infragravity-wave heights. The incoming infragravity wave is clearly influenced by the bed slope. While propagating over the 1:80 slope, the infragravity waves grow higher than over the 1:20 slope, as during the longer propagation time on the 1:80 slope, more energy can be transferred. The growth in infragravity-wave height is also depth dependent, as triad interactions are closer to resonance in shallow water, and thus allow for stronger energy transfers. The depth-dependent growth can be observed for example in the first 5 m after the slope change ($45 < x < 50$ m). On the 1:20 slope, where the water depth shallows relatively fast, infragravity waves grow faster in height than on the 1:80 slope, where the water depth is comparatively deeper. An interesting feature is that while the incoming infragravity-wave heights differ considerably depending on the profile, the outgoing infragravity-wave heights are very similar, indicating substantially different reflections. Interestingly, at $H_{IG}/h \approx$ 0.4–0.45 the infragravity waves start to dissipate energy at all three cases. This value is similar to sea-swell dissipation, which starts here for all three cases at $H_{SW}/h \approx$ 0.4–0.45. The earlier described decrease and subsequent increase in both incoming and outgoing infragravity-wave height, observed to be frequency dependent, is more pronounced on steeper slopes, which is most likely caused by the stronger reflection on those profiles.

The power spectra (Figure 7) in the shoaling zone (at $h = 25$ cm) contain a clear spectral peak with a number of higher harmonics. In the outer surf zone ($h = 12.5$ cm) the spectral peak and its harmonics start to decrease. In the inner surf zone ($h = 5$ cm), the spectra vary substantially between the profiles. While on the 1:80 slope the sea-swell energy has largely dissipated and infragravity frequencies dominate, the offshore spectral peak and its harmonics are still present and dominate over infragravity frequencies on the 1:20 slope.

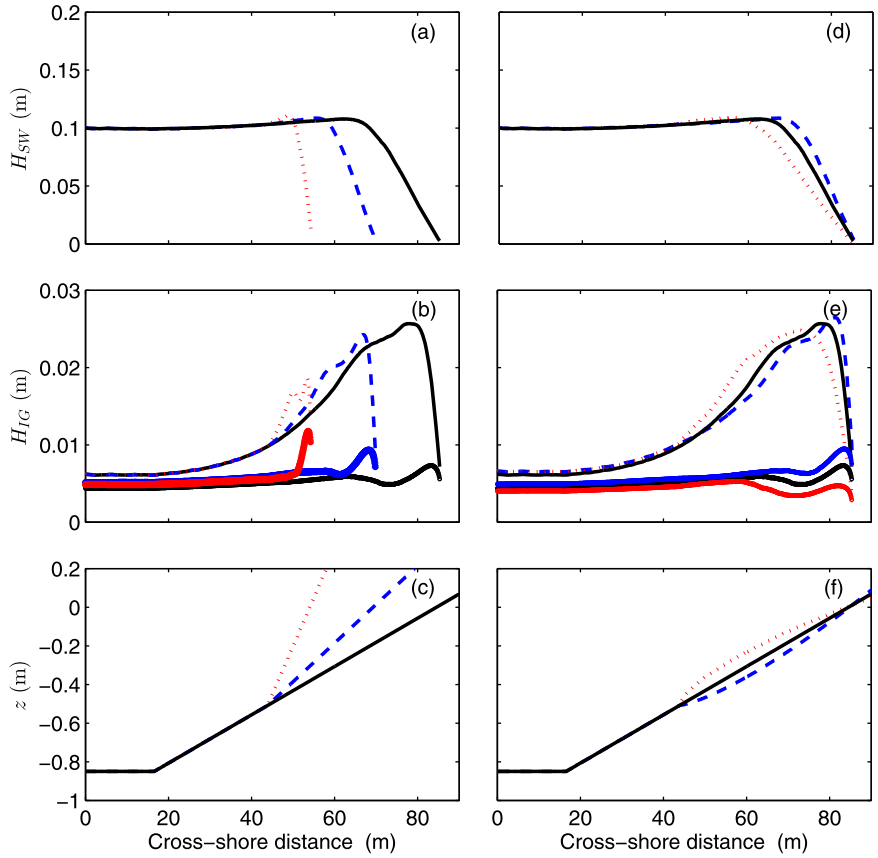

Figure 6. Significant (a, d) sea-swell H_{SW} and (b, e) infragravity H_{IG} wave heights with (c, f) corresponding bathymetries. For Figures 6a–6c a 1:20 (red dotted line), 1:50 (blue dashed line), and 1:80 sloping profile (black solid line), and (d–f) with a concave (blue dashed line), a convex (red dotted line) and a uniform 1:80 sloping profile (black solid line).

Figures 8a–8c show the imaginary part of the bispectrum on three locations in the sea-swell surf zone for the 1:20 slope. Here, interactions between infragravity frequencies are present from just before the onset of infragravity-wave dissipation onward (Figure 8b) (infragravity-wave dissipation starts at $x > 53.5$ m), and do not dominate anywhere. This contrasts with the 1:80 slope, as seen previously in the validation section, where interactions between infragravity frequencies are already present within the first part of the sea-swell surf zone (Figures 4b and 4e). Two other interaction patterns dominate during the infragravity-wave energy dissipation (Figure 8c). One is the negative band ranging from about $B(0.22,0.22)$ to $B(0.44,0)$, where energy is transferred from the spectral peak to frequencies lower than the spectral peak, including infragravity frequencies. The other is a positive band ranging from $B(0.44,0)$ to $B(0,44,0.44)$ where energy is transferred to frequencies higher than the spectral peak by interactions between the spectral peak and frequencies lower than the spectral peak, including infragravity frequencies. For the 1:50 slope the first part of the infragravity-wave dissipation (67 m $< x <$ 68 m) has interactions similar to the 1:20 slope (compare Figure 8e with Figure 8b), but is also showing interactions between infragravity frequencies only. Most of the decrease in infragravity-wave height is between 68 m $< x <$ 70 m, where only infragravity self-self interactions are present (Figure 8f).

The four nonlinear source terms calculated for the 1:20 slope are visible in Figure 9. The narrow surf zone results in a more compressed energy transfer field in the cross-shore compared to the 1:80 slope (Figure 5) and the harmonics are more distinct, but overall $S_{nl,III}$ and $S_{nl,IV}$ (Figures 9c and 9d) are very similar to the 1:80 slope. On the contrary, the $S_{nl,I}$ and $S_{nl,II}$ terms (Figures 9a and 9b) are generally much weaker than on the 1:80 slope. This might be explained by the relative importance of infragravity waves compared to sea-swell waves in shallow water; in a water depth of 5 cm, on the 1:20 slope $H_{IG}^{+}/H_{SW} = 0.34$ versus 0.79 for the 1:80 slope (the H_{IG}^{+}/h ratio did not differ considerably, with 0.37 for the 1:20 slope, and 0.49 for both the 1:50 and 1:80 slopes). As a result, infragravity waves may not self-interact as strongly on steep slopes. As

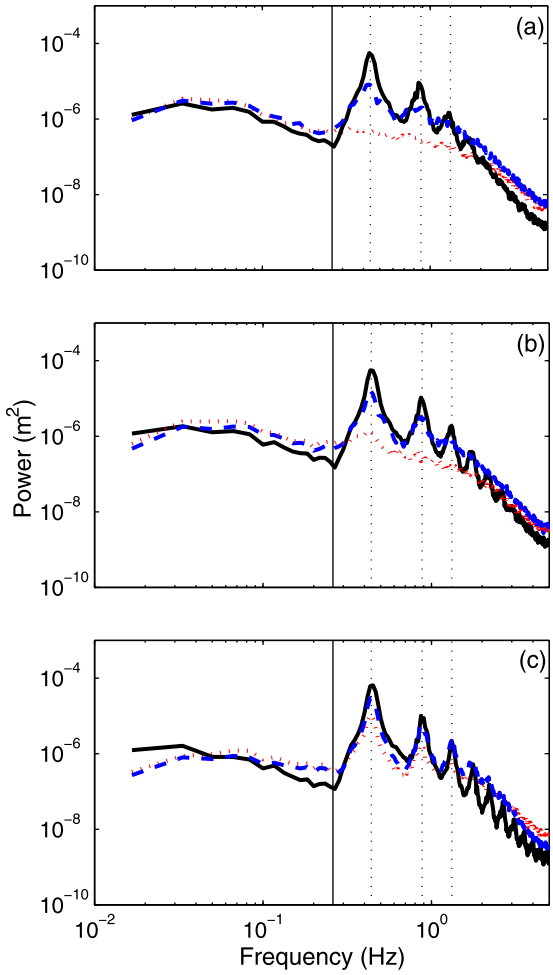

Figure 7. Modeled power spectra for *A*3, for a (a) 1:80 slope, (b) 1:50 slope, and (c) 1:20 slope at three cross-shore locations. Shoaling ($h = 25$ cm, black solid line), outer surf ($h = 12.5$ cm, blue dashed line) and inner surf zone ($h = 5$ cm, red dotted line). The vertical solid line indicates the cutoff between infragravity and sea-swell wave frequencies. Vertical dashed lines indicate offshore power spectral peak ($f = 0.44$ Hz) and the first ($f = 0.88$ Hz) and second ($f = 1.32$ Hz) harmonic.

seen earlier in the bispectra (Figures 8b and 8c), $S_{nl,I}$ interactions are generally weak, and while $S_{nl,II}$ interactions do show the transfer of energy toward infragravity frequencies, the reversal of the transfers (as seen for the 1:80 slope) where energy goes from infragravity frequencies to what might be called a higher infragravity-wave harmonic within the sea-swell frequency range, is not visible. The infragravity-wave energy loss is solely caused by $S_{nl,III}$ interactions (Figure 9c). This indicates that the positive band ranging from *B*(0.44,0) to *B*(0,44,0.44) in the bispectra (Figure 8c) must dominate over the negative band ranging from about *B*(0.22,0.22) to *B*(0.44,0) during infragravity-wave energy dissipation.

In short, these results show two distinctive interaction-patterns during infragravity-wave energy dissipation that vary with importance depending on the steepness of the profile. On a low-sloping beach, where infragravity-wave energy is relatively important, infragravity-infragravity interactions dominate and seem to generate infragravity higher harmonics, suggesting infragravity-wave breaking. On a steep-sloping beach, where sea-swell waves dominate everywhere, infragravity frequencies interact with the spectral peak and energy is spread to a wide range of higher frequencies.

3.2. Convex Versus Concave

To study the effect of the beach shape, rather than steepness, on the energy transfers, the 1:80 profile is changed into a concave ($x^{4/3}$) and convex ($x^{2/3}$) shape (Figures 6d–6f). For the convex shape, this causes the location of the sea-swell surf zone to shift slightly more seaward, due to the somewhat steeper local slope. As the convex shape is also somewhat steeper in the shoaling zone, water depth is in general shallower. This causes a stronger growth rate of both the sea-swell and infragravity wave height compared to the uniform profile over the same distance, but in total a smaller maximum infragravity-wave height further landward. The milder local slope in the inner surf zone of the convex profile causes the infragravity wave to dissipate slightly more energy than on the uniform profile, as deduced from the different outgoing wave heights close to the shore (Figure 6e). Figure 10 shows the four nonlinear source terms for the convex profile versus cross-shore distance. On the whole, all four terms are very similar to the 1:80 uniform slope (Figure 5), other than having a slightly wider cross-shore zone with less intense interactions. The results for the concave profile are opposite to those of the convex profile, with weaker, longer shoaling with a higher maximum infragravity-wave height and weaker energy dissipation (Figure 6e). Nonlinear source terms for the concave profile (not shown) are also very similar to the uniform profile but occur in a more narrow cross-shore zone and have, in general, more intense interactions.

Overall, the interaction patterns on the convex and concave beach profiles are not substantially different from a uniform profile. The strength of the interactions, however, does vary, with stronger transfers over a convex slope, confirming the observations of *Thomson et al.* [2006]. This can be explained by the relatively

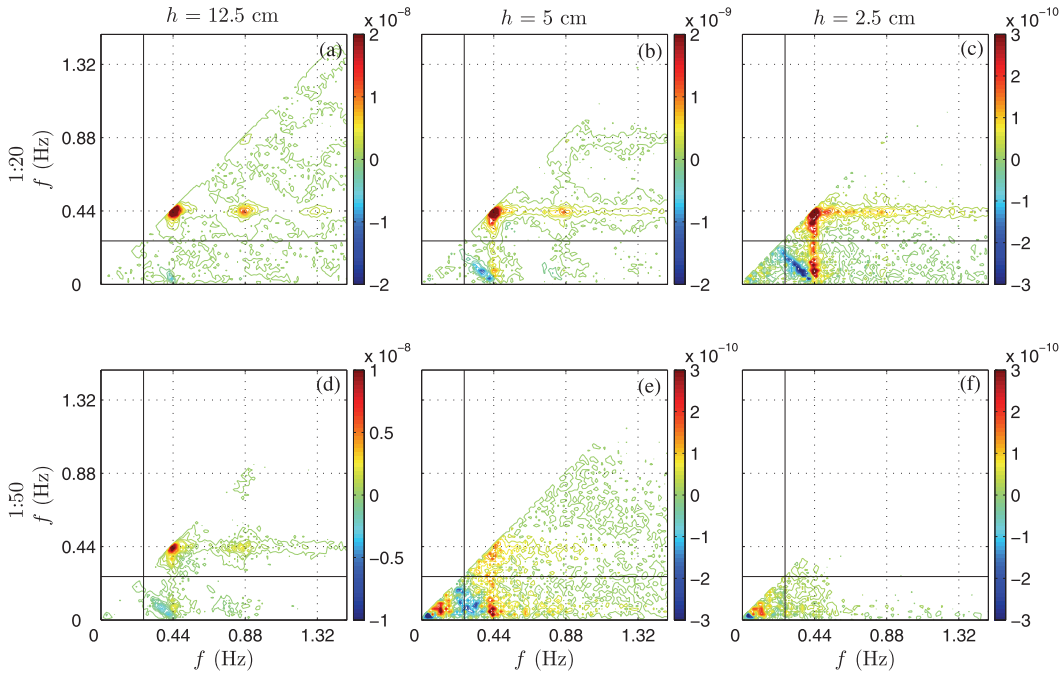

Figure 8. Imaginary part of the bispectrum of the incoming wave signal (η^+) for *A*3 over the (a–c) 1:20 slope and (d–f) 1:50 slope for values where $b^2 > b_{95\%}$. Dashed lines indicate the spectral peak ($f = 0.44$ Hz) and its higher harmonics. In water depth *h* of (a, d) 12.5 cm (1:20 slope, $x = 51.6$ m, 1:50 slope $x = 63.1$ m), (b, e) 5 cm (1:20 slope, $x = 53.2$ m, 1:50 slope $x = 67.1$ m) and (c, f) 2.5 cm (1:20 slope, $x = 53.8$ m, 1:50 slope $x = 68.5$ m).

shallower water depths on the convex profile, where triad interactions are closer to resonance. This enhances energy exchanges, leading to slightly stronger infragravity-wave energy dissipation.

3.3. Other Wave Conditions

In addition to the beach profile, the offshore wave conditions may affect the strength of nonlinear interactions too [e.g., *Elgar and Guza*, 1985; *Herbers et al.*, 1994]. Therefore, we also ran the broad-banded mild-energetic condition *A*1 and high-energetic condition *A*2 over the 1:20, 1:50 and 1:80 slopes. Significant wave heights are given in Figure 11. As can be seen, the surf zone width changes with the offshore wave height; for each case the surf zone commences near $H_{SW}/h \approx 0.4$–0.45. Also for these broad-banded conditions, the maximum infragravity-wave height depends on the bed slope (Figures 11b and 11e), but considerably less so than for the narrow-banded *A*3 case (Figure 6b). Infragravity-wave dissipation starts at $H_{IG}/h = 0.4$–0.5 for the 1:50 and 1:80 slopes, and at ≈ 0.65 for the 1:20 slopes. Clearly, the outgoing infragravity-wave heights are larger on the 1:20 slope, indicating stronger reflection from the shoreline.

Case *A*1 shows overall the same trends in nonlinear energy transfers as case *A*3, but with weaker transfers that are spread over a wider frequency range (not shown). Case *A*2 shows relatively stronger transfers that are spread over a wider cross-shore zone, and wider frequency range compared to *A*3; see for example the results for case *A*2 on the 1:80 slope in Figure 12 (note the different color scale compared to previous figures). Interestingly, energy is first transferred from high to low infragravity frequencies by $S_{nl,I}$ interactions (Figure 12a) (not seen for case *A*1 and *A*3). For $x \approx 70$ m onward the $S_{nl,I}$ interactions become stronger and are reversed. In addition, infragravity frequencies loose energy from $x \approx 65$ m onward through $S_{nl,III}$ interactions while still receiving energy through $S_{nl,II}$ interactions (Figures 12b and 12c). This is reflected in the incoming infragravity wave height H_{IG}^{+}, which stays more or less constant around $x \approx 65$–70 m (Figure 11e), but decreases slowly from $x \approx 70$ m onward. When $S_{nl,I}$ and $S_{nl,II}$ terms show a transfer to higher frequencies, the infragravity-wave height decreases at a much quicker rate. This latter trend can be identified for all other wave conditions as well, although less pronounced.

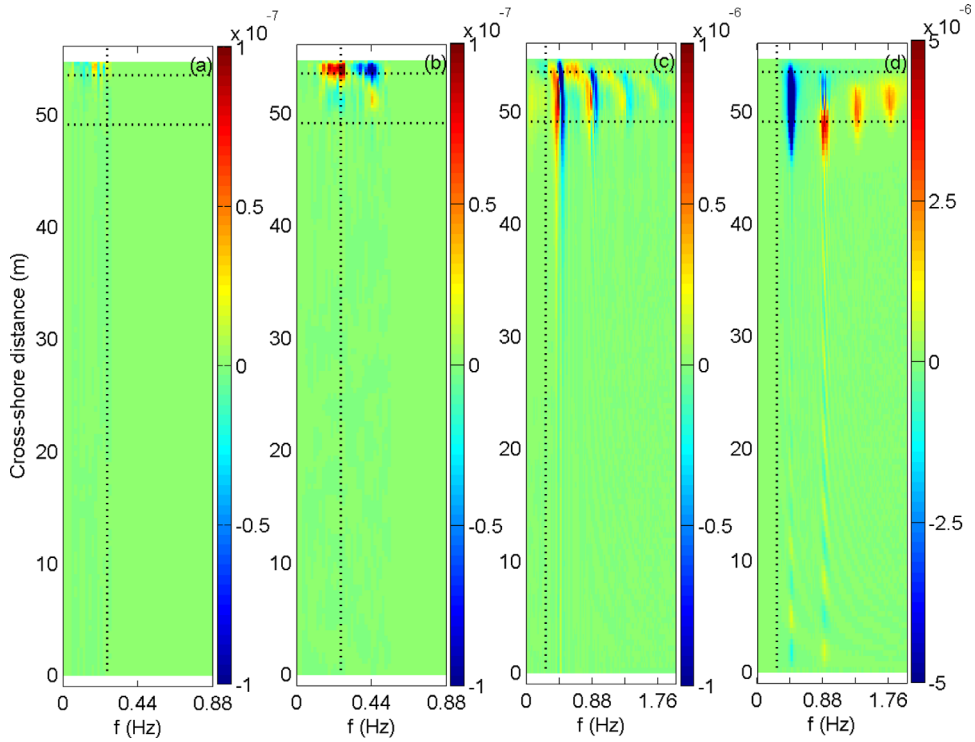

Figure 9. Nonlinear source term S_{nl} estimated from the modeled incoming wave signal of case *A*3 on the 1:20 slope, versus frequency *f* and cross-shore position *x*. With (a) infragravity frequencies only ($S_{nl,I}$), (b) two infragravity and one sea-swell frequency ($S_{nl,II}$), (c) two sea-swell and one infragravity frequency ($S_{nl,III}$) and (d) sea-swell frequencies only ($S_{nl,IV}$). The vertical solid line indicates the cutoff between infragravity and sea-swell wave frequencies. The horizontal dashed lines indicate the locations of the maximum infragravity ($x = 53.4$ m) and sea-swell ($x = 49.0$ m) wave heights just before dissipation starts.

4. Discussion

The shoreward propagating infragravity waves experienced considerable energy loss in all simulations, causing reflection to be incomplete. To evaluate the influence of the bed slope on the amount of reflection, we explored the dependence of the reflection coefficients *R* (defined below) of all *A*3 simulations on the normalized bed slope [*Van Dongeren et al*., 2007]

$$M_{H,IG} = \frac{MT_{IG}}{2\pi}\sqrt{\frac{g}{H_{IG}^{+}}} \tag{7}$$

where *M* is the local bed slope, T_{IG} is the infragravity-wave period and H_{IG}^{+} is the incoming infragravity-wave height. The normalized bed slope parameter is based on the concept that a given slope appears steeper to longer (lower frequency) waves than it does to shorter (higher frequency) waves. *Van Dongeren et al*. [2007] defined, based on bichromatic wave simulations, a mild-sloping regime ($M_{H,IG} < 1.25$), where infragravity waves loose a large part of their energy by breaking, and a steep-sloping regime ($M_{H,IG} > 1.25$), where infragravity waves almost fully reflect. This transition at $M_{H,IG} \approx 1.25$ is similar to the value previously found for the onset of sea-swell wave breaking by *Battjes* [1974]. *R* and $M_{H,IG}$ were determined here at a water depth of 5 cm (equivalent to $h = 1$ m in the field) for $f = 0.01$–0.25 Hz with a stepsize of 0.015 Hz. The local bed slope, *M* is determined here as the average slope between 1 m seaward and 1 m shoreward of the selected cross-shore position with $h = 5$ cm. The local incoming infragravity-wave height was estimated as $H_{IG}^{+} = 4\sqrt{\int_{f-\Delta f}^{f+\Delta f} E^{+}(f)df}$, with a frequency resolution Δf of 0.00111 Hz. Here E^{+} is calculated following *Sheremet et al*. [2002],

$$E^{\pm}(f) = \frac{1}{4}\left[Co_{\eta\eta}(f) + \frac{h}{g}Co_{uu}(f) \pm \left(2\sqrt{\frac{h}{g}}\right)Co_{\eta u}(f)\right], \tag{8}$$

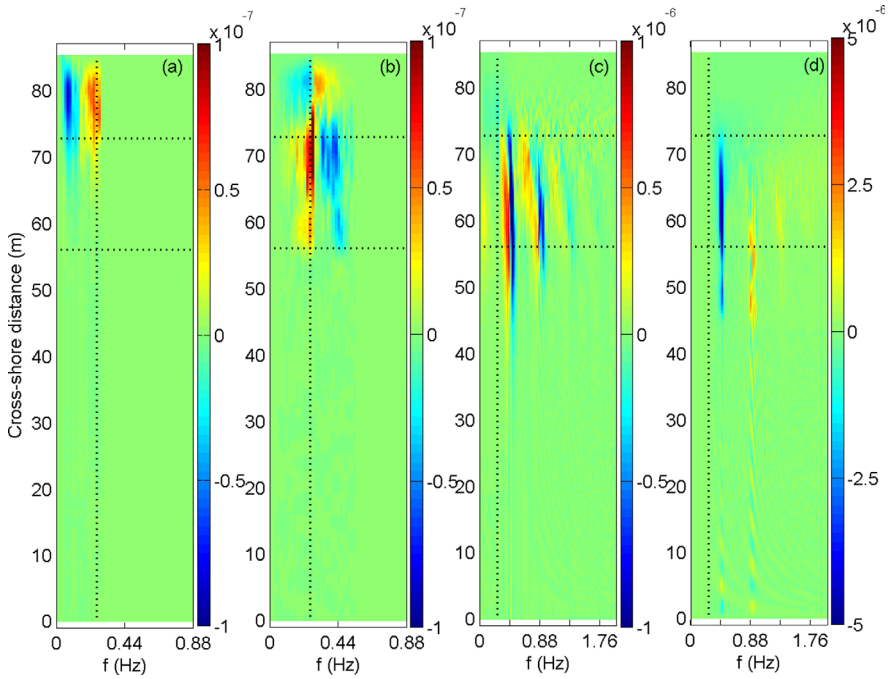

Figure 10. Nonlinear source term S_{nl} estimated from the modeled incoming wave signal of case *A*3 on the convex slope, versus frequency *f* and cross-shore position *x*. With (a) infragravity frequencies only ($S_{nl,I}$), (b) two infragravity and one sea-swell frequency ($S_{nl,II}$), (c) two sea-swell and one infragravity frequency ($S_{nl,III}$), and (d) sea-swell frequencies only ($S_{nl,IV}$). The vertical solid line indicates the cutoff between infragravity and sea-swell wave frequencies. The horizontal dashed lines indicate the locations of the maximum infragravity ($x = 72.7$ m) and sea-swell ($x = 56.0$ m) wave heights just before dissipation starts.

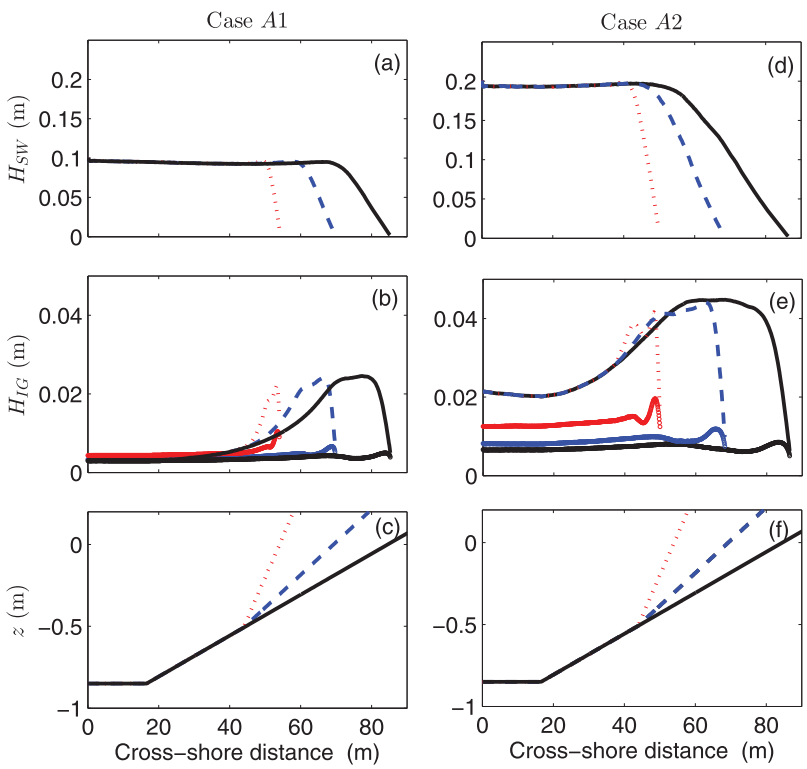

Figure 11. Significant (a, d) sea-swell H_{SW} and (b, e) incoming and outgoing infragravity H_{IG} wave heights with (c, f) corresponding bathymetries for (left) case *A*1 and (right) case *A*2. For a 1:20 (red dotted line), 1:50 (blue dashed line) and 1:80 sloping profile (black solid line).

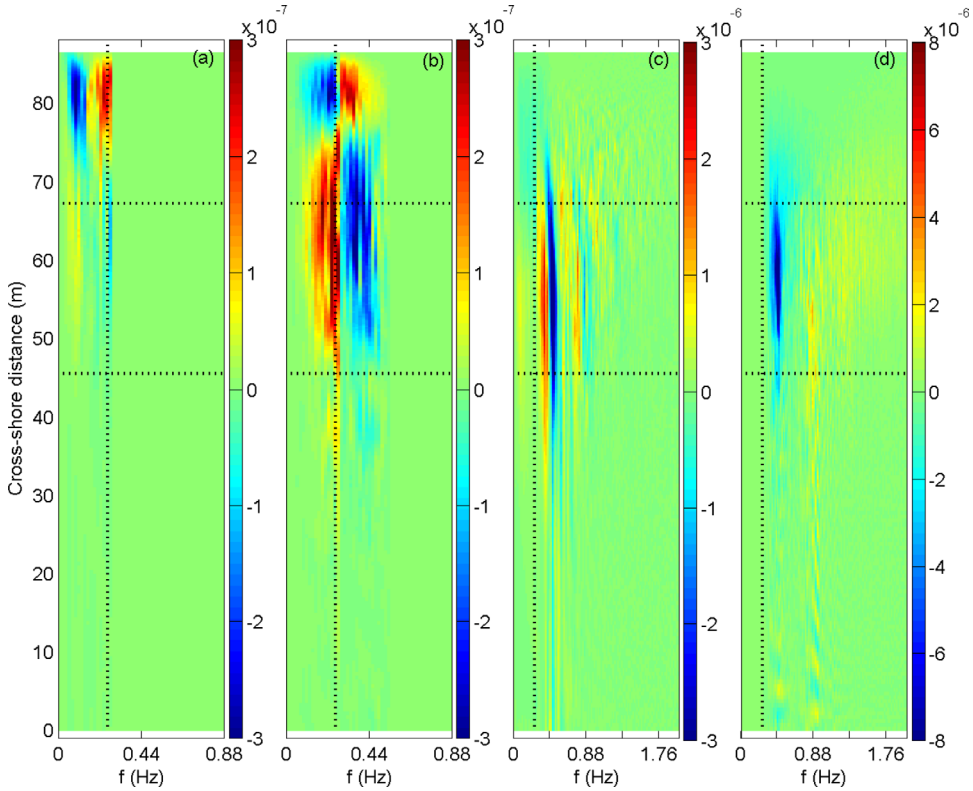

Figure 12. Nonlinear source term S_{nl} estimated from the modeled incoming wave signal of case *A*2 on a 1:80 slope, versus frequency *f* and cross-shore position *x*. With (a) infragravity frequencies only ($S_{nl,I}$), (b) two infragravity and one sea-swell frequency ($S_{nl,II}$), (c) two sea-swell and one infragravity frequency ($S_{nl,III}$), and (d) sea-swell frequencies only ($S_{nl,IV}$). The vertical solid line indicates the cutoff between infragravity and sea-swell wave frequencies. The horizontal dashed lines indicate the locations of the maximum infragravity ($x = 67.1$ m) and sea-swell ($x = 45.5$ m) wave heights just before dissipation starts.

where $Co_{\eta u}$ is the $\eta - u$ cospectrum and $Co_{\eta\eta}$ and Co_{uu} are η and u autospectra. R is defined as $R(f) = \sqrt{F^-(f)/F^+(f)}$ with $F^{\pm}(f) = E^{\pm}(f)\sqrt{gh}$.

Figure 13 shows a clear correlation of the frequency dependent $R(f)$ with $M_{H,IG}$. Estimating the parameters at the location of maximum infragravity-wave height gives similar results (not shown). The transition from the mild-sloping to the steep-sloping regime is here at $M_{H,IG} \approx 4$, where $R < 0.75$. This value is similar to observations of *De Bakker et al.* [2014] on mild to steep sloping natural beaches where $M_{H,IG} \approx 3$. The 1:80 slope has predominantly low R and $M_{H,IG}$ values, and is mostly within the mild sloping regime, whereas the 1:20 slope has overall larger R and $M_{H,IG}$ values and is for a large part within the steep sloping regime (Figure 13a). Cases *A*1 and *A*2 demonstrate the same behavior (not shown). The fact that the 1:20 slope has a similar dependence on the normalized bed slope $M_{H,IG}$ as the milder slopes is remarkable. Following Van Dongeren's reasoning, this would indicate that on steep sloping beaches, although infragravity self-self interactions are weak, the highest infragravity frequencies experience breaking. The convex and concave profiles are very similar to the uniform 1:80 profile (Figure 13b), with only slightly larger R and $M_{H,IG}$ for the concave profile than for the uniform and convex profiles.

If the infragravity waves would experience breaking, one would expect the wave shape to become skewed, and subsequently asymmetric just before the onset of energy dissipation, similar to sea-swell waves. To shed more light on the infragravity-wave shapes during dissipation, the infragravity-wave integrated biphases are shown in Figure 14. A biphase of 0° is indicative of a skewed wave shape, whereas a biphase of −90° indicates an asymmetric wave shape [e.g., *Masuda and Kuo*, 1981; *Elgar and Guza*, 1985; *Elgar*, 1987]. Biphases (β_{f_1,f_2}) were integrated over the infragravity (β_{IG}, zone I) frequency band as,

$$\beta_{IG} = \arctan\left[\frac{\mathcal{I}\{\sum_{f_1=0}^{f_{IG}}\sum_{f_2=0}^{f_{IG}}\{B_{f_1,f_2}\}\}}{\mathcal{R}\{\sum_{0}^{f_{IG}}\sum_{0}^{f_{IG}}\{B_{f_1,f_2}\}\}}\right]. \quad (9)$$

The graph shows that on the mild 1:80 profile, the infragravity biphases evolve from ≈ 180° outside of the sea-swell surf zone to a positively skewed wave ($\beta_{IG} = 0°$) and eventually to a more sawtooth shaped wave with $\beta_{IG} = -50°$ close to shore, where zone I interactions are prominent. This shape evolution was reported earlier for the GLOBEX laboratory data set by *Rocha et al.* [2013]. On the 1:50 profile, the infragravity-wave transformation takes place over a shorter cross-shore distance and only a few meters from the shoreline the infragravity-wave becomes more asymmetric, with $\beta_{IG} \approx -25°$. On the steep 1:20 profile, the infragravity wave does not develop an asymmetric shape, as the β_{IG} evolves only to ≈ 0°, indicating a skewed wave shape.

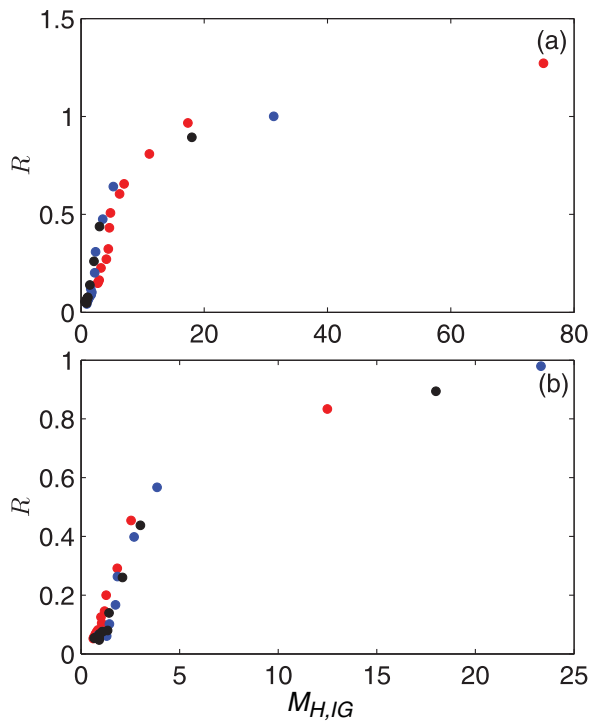

Figure 13. Amplitude reflection coefficient R versus normalized bed slope $M_{H,IG}$ for case $A3$ at $h = 5$ cm. The dots represent $f = 0.01$–0.25 Hz, with a 0.015 Hz step size. For (a) a 1:80 (black dots), 1:50 (blue dots) and 1:20 sloping profile (red dots), and (b) a uniform (black dots), concave (blue dots) and convex 1:80 sloping profile (red dots). With f = 0.01 Hz in the top right of the plot and f = 0.25 Hz in the lower left.

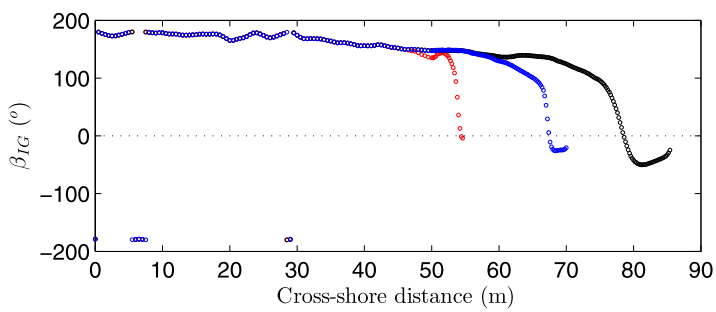

Figure 14. Biphases integrated over the infragravity frequency band (zone I) for the incoming wave signal of case $A3$ for values where $b^2 > b_{95}$, for the 1:80 (black dots), the 1:50 (blue dots) and the 1:20 sloping profile (red dots).

To summarize, in shallow water on a mild 1:80 slope, where the infragravity-wave energy dominates the water motion, infragravity-infragravity interactions generate higher harmonics and the infragravity wave becomes asymmetric. The infragravity-wave reflection coefficient depends on the normalized bed slope. Altogether, this is similar to sea-swell wave behavior, and suggest the breaking of infragravity waves in the inner surf zone. On the contrary, on a steep 1:20 slope, where infragravity-wave energy is relatively small, infragravity-infragravity interactions are weak, and the infragravity wave does not become asymmetric. During infragravity-wave dissipation, energy is spread to a wide range of higher frequencies through interactions with the spectral peak. Nonetheless, the reflection coefficient depends on the normalized bed slope, similar to milder slopes.

5. Conclusions

Using the nonhydrostatic SWASH model we studied energy transfer patterns for a diverse set of beach profiles and wave conditions with a focus on infragravity frequencies. The model validation, with a high-resolution laboratory data set on a gently sloping beach, shows that SWASH is capable of modeling the detailed nonlinear interactions. We observe that especially the beach slope affects the nonlinear

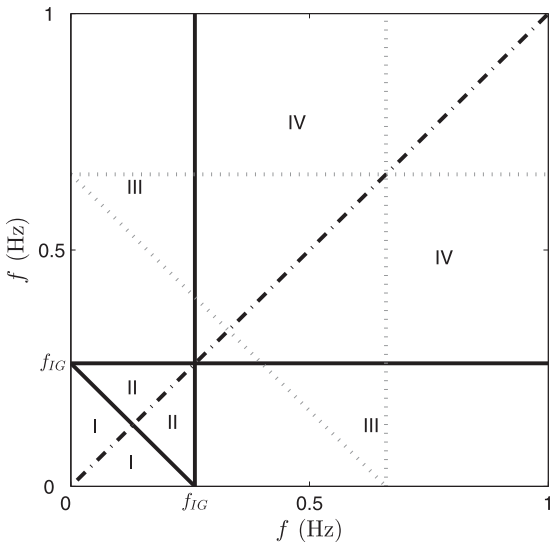

Figure 15. Bispectrum separated into four zones by solid lines from *De Bakker et al*. [2015]. Zone I contains infragravity frequencies only, zone II two infragravity and one sea-swell frequency, zone III two sea-swell and one infragravity frequency and zone IV, sea-swell frequencies only. The present figure shows the case *A3*, with $f_{IG} = 0.26$ Hz. The black dash-dotted line indicates the symmetry of the bispectra. The grey dotted lines indicate the integration for an example frequency $f = 0.66$ Hz, consisting of three branches, a diagonal branch for sum interactions (S_{nl}^{+}) and horizontal and vertical branches for difference interactions (S_{nl}^{-}).

infragravity-wave interactions. In shallow water on a low-sloping beach, where infragravity-wave energy dominates the water motion, infragravity-infragravity interactions are well developed and generate higher harmonics. This leads to the steepening and eventually the breaking of the infragravity waves, and large energy losses. On the contrary, on a steep-sloping beach, sea-swell waves dominate everywhere. Infragravity frequencies interact with the spectral peak and spread energy to a wide range of higher frequencies, with relatively less infragravity-energy dissipation. Although both beach types have two distinct nonlinear interaction patterns during infragravity-wave energy dissipation, the frequency-dependent reflection can be estimated by a single parameter, the normalized bed slope.

Appendix A: Nonlinear Energy Transfers

Here we use the stochastic formulation of the second-order nonlinear wave interaction theory of *Herbers et al*. [2000, equation (4)] to determine S_{nl} discretely by:

$$S_{nl,f} = \frac{3\pi(f)}{h}\mathcal{I}\left\{\left(\sum_{f'=0}^{f} B_{f',f-f'} - 2\sum_{f'=0}^{\infty} B_{f',f}\right)\right\}, \tag{A1}$$

where f and f' are two variable frequencies, and where the imaginary part of the bispectrum represents the energy transfers and is integrated in two parts. The term $\sum_{f'=0}^{f} B_{f',f-f'}$ accounts for the sum interactions in the bispectrum, and the term $-2\sum_{f'=0}^{\infty} B_{f',f}$ accounts for the difference interactions.

To obtain more insight in the different types of triad interactions, the bispectrum is divided into four zones, following *De Bakker et al*. [2015], see Figure 15. The three involved frequencies (f_1, f_2, f_3) are depicted in the bispectral plane with f_1 along the horizontal axis, f_2 along the vertical axis and f_3 as the sum of f_1 and f_2. Interactions including infragravity frequencies only are defined as zone I; zone II involves two infragravity and one sea-swell wave frequencies; zone III includes one infragravity and two sea-swell wave frequencies; and, zone IV includes solely sea-swell wave frequencies. The integration over the four zones separately is performed as described in *De Bakker et al*. [2015], their Appendix A.

Acknowledgments
The laboratory data can be made available upon request from the first author (a.t.m.debakker@uu.nl). This work was funded by the Netherlands Organisation for Scientific Research (NWO) under contract 821.01.012. The GLOBEX project was coordinated by Hervé Michallet (LEGI, Université de Grenoble) and Gerben Ruessink (Utrecht University) and supported by the European Community's Seventh Framework Programme through the Hydralab IV project, EC Contract 261520. The authors thank all fellow researchers and Deltares employees involved in the project. The authors also like to thank Pieter Smit for his help with the SWASH model set-up, and Tom Herbers for his advice during the initial part of this work. The many discussions with Jantien Rutten, Joost Brinkkemper and Timothy Price, as well as comments made by two reviewers, helped to compose this work further.

References

Battjes, J. A. (1974), Surf similarity, in *Proceedings of the 14th International Conference on Coastal Engineering*, edited by B.Edge, pp. 466–480, Am. Soc. Civ. Eng., Reston, Va

Battjes, J. A., H. J. Bakkenes, T. T. Janssen, and A. R. van Dongeren (2004), Shoaling of subharmonic gravity waves, *J. Geophys. Res.*, *109*, C02009, doi:10.1029/2003JC001863.

Chow, V. T. (1959), *Open Channel Hydraulics*, McGraw-Hill, N. Y.

Collis, W., P. White, and J. Hammond (1998), Higher-order spectra: The bispectrum and trispectrum, *Mech. Syst. Signal Process.*, *12*(3), 375–394.

De Bakker, A., M. Tissier, and B. G. Ruessink (2014), Shoreline dissipation of infragravity waves, *Cont. Shelf Res.*, *72*, 73–82.

De Bakker, A., T. Herbers, P. Smit, M. Tissier, and B. G. Ruessink (2015), Nonlinear infragravity-wave interactions on a gently sloping laboratory beach, *J. Phys. Oceanogr.*, *45*, 589–605.

Elgar, S. (1987), Relationships involving third moments and bispectra of a harmonic process, *IEEE Trans. Acoust. Speech Signal Process.*, *35*, 1725–1726.

Elgar, S., and R. T. Guza (1985), Observations of bispectra of shoaling surface gravity waves, *J. Fluid Mech.*, *161*, 425–448.

Freilich, M. H., and R. Guza (1984), Nonlinear effects on shoaling surface gravity waves, *Philos. Trans. R. Soc. London A*, *311*, 1–41.

Guedes, M., K. R. Bryan, and G. Coco (2013), Observations of wave energy fluxes and swash motions on a low-sloping, dissipative beach, *J. Geophys. Res. Oceans*, *118*, 3651–3669, doi:10.1002/jgrc.20267.

Guza, R., E. Thornton, and R. Holman (1984), Swash on steep and shallow beaches, in *Proceedings of the 19th International Conference on Coastal Engineering*, pp. 708–723, Am. Soc. of Civ. Eng., Reston, Va

Guza, R. T., and E. B. Thornton (1982), Swash oscillations on a natural beach, *J. Geophys. Res.*, *87*, 483–491.

Hasselmann, K., W. Munk, and G. MacDonald (1963), Bispectra of ocean waves, in *Time Series Analysis*, edited by M. Rosenblatt, pp. 125–139, John Wiley, N. Y.

Henderson, S. M., R. T. Guza, S. Elgar, T. H. C. Herbers, and A. J. Bowen (2006), Nonlinear generation and loss of infragravity wave energy, *J. Geophys. Res.*, *111*, C12007, doi:10.1029/2006JC003539.

Herbers, T., and M. Burton (1997), Nonlinear shoaling of directionally spread waves on a beach, *J. Geophys. Res.*, *102*, 21,101–21,114.

Herbers, T., N. Russnogle, and S. Elgar (2000), Spectral energy balance of breaking waves within the surf zone, *J. Phys. Oceanogr.*, *30*, 2723–2737.

Herbers, T. H. C., S. Elgar, and R. T. Guza (1994), Infragravity-frequency (0.005-0.05 Hz) motions on the shelf. Part I: Forced waves, *J. Phys. Oceanogr.*, *24*, 917–927.

Herbers, T. H. C., S. Elgar, and R. Guza (1995a), Generation and propagation of infragravity waves, *J. Geophys. Res.*, *100*, 24,863–24,872.

Herbers, T. H. C., S. Elgar, R. Guza, W. C. O'Reilly (1995b), Infragravity-frequency (0.005-0.05 hz) motions on the shelf. Part II: Free waves, *J. Phys. Oceanogr.*, *25*, 1063–1079.

Kim, Y., and E. Powers (1979), Digital bispectral analysis and its application to nonlinear wave interactions, *IEEE Trans. Plasma Sci.*, *1*, 120–131.

Lin, Y. H., and H. H. Hwung (2012), Infra-gravity wave generation by the shoaling wave groups over beaches, *China Ocean Eng.*, *26*, 1–18.

Longuet-Higgins, M. S., and R. W. Stewart (1962), Radiation stress and mass transport in gravity waves, with application to 'surf beats,' *J. Fluid Mech.*, *13*, 481–504.

Masuda, A., and Y. Y. Kuo (1981), A note on the imaginary part of bispectra, *Deep Sea Res., Part A*, *28*(3), 213–222.

Norheim, C., T. Herbers, and S. Elgar (1998), Nonlinear evolution of surface wave spectra on a beach, *J. Phys. Oceanogr.*, *28*, 1534–1551.

Pomeroy, A., R. Lowe, G. Symonds, A. Van Dongeren, and C. Moore (2012), The dynamics of infragravity wave transformation over a fringing reef, *J. Geophys. Res.*, *117*, C11022, doi:10.1029/2012JC008310.

Rijnsdorp, D. P., P. Smit, and M. Zijlema (2012), Non-hydrostatic modelling of infragravity waves using swash, in *Proceedings of the 33rd International Conference on Coastal Engineering*, edited by P. J. Lynett, and J. M. Smith, pp. 1–12, World Scientific Publishing, Singapore.

Rijnsdorp, D. P., B. G. Ruessink, and M. Zijlema (2015), Infragravity-wave dynamics in a barred coastal region, a numerical study, *J. Geophys. Res. Oceans*, *120*, 4068–4089, doi:10.1002/2014JC010450.

Rocha, M., H. Michallet, P. Silva, A. Tiago, and E. Bartélemy (2013), Nonlinearities of short and long waves across the shoaling, surf and swash zones: Physical model results, in *Proceedings of 7th International Conference on Coastal Dynamics*, pp. 1329–1340, Am. Soc. of Civ. Eng., Reston, Va.

Ruessink, B. G. (1998), Bound and free infragravity waves in the nearshore zone under breaking and nonbreaking conditions, *J. Geophys. Res.*, *103*, 12,795–12,805.

Ruessink, B. G., H. Michallet, P. Bonneton, D. Mouazé, J. Lara, P. Silva, and P. Wellens (2013), Globex: Wave dynamics on a gently sloping laboratory beach, in *Proceedings of Coastal Dynamics 2013*, pp. 1351–1362, Am. Soc. of Civ. Eng., Reston, Va.

Ruju, A., J. Lara, and I. Losada (2012), Radiation stress and low-frequency energy balance within the surf zone: A numerical approach, *Coastal Eng.*, *68*, 44–55.

Ruju, A., J. Lara, and I. Losada (2014), Numerical analysis of run-up oscillations under dissipative conditions, *Coastal Eng.*, *86*, 45–56.

Russell, P. (1993), Mechanisms for beach erosion during storm, *Cont. Shelf Res.*, *13*, 1243–1265.

Sénéchal, N., G. Coco, K. R. Bryan, and R. A. Holman (2011), Wave runup during extreme storm conditions, *J. Geophys. Res.*, *116*, C07032, doi:10.1029/2010JC006819.

Sheremet, A., R. T. Guza, S. Elgar, and T. H. C. Herbers (2002), Observations of nearshore infragravity waves: Seaward and shoreward propagating components, *J. Geophys. Res.*, *107*(C8), 3095, doi:10.1029/2001JC000970.

Smit, P., M. Zijlema, and G. Stelling (2013), Depth-induced wave breaking in a non-hydrostatic, near-shore wave model, *Coastal Eng.*, *76*, 1–16.

Smit, P., T. Janssen, L. Holthuijsen, and J. Smith (2014), Non-hydrostatic modeling of surf zone wave dynamics, *Coastal Eng.*, *83*, 36–48.

Thomson, J., S. Elgar, B. Raubenheimer, T. H. C. Herbers, and R. T. Guza (2006), Tidal modulation of infragravity waves via nonlinear energy losses in the surfzone, *Geophys. Res. Lett.*, *33*, L05601, doi:10.1029/2005GL025514.

Van Dongeren, A., J. Battjes, T. Janssen, J. van Noorloos, K. Steenhauer, G. Steenbergen, and A. Reniers (2007), Shoaling and shoreline dissipation of low-frequency waves, *J. Geophys. Res.*, *112*, C02011, doi:10.1029/2006JC003701.

Van Dongeren, A., R. Lowe, A. Pomeroy, D. Trang, D. Roelvink, G. Symonds, and R. Ranasinghe (2013), Numerical modeling of low-frequency wave dynamics over a fringing coral reef, *Coastal Eng.*, *73*, 178–190.

Van Thiel de Vries, J. S. M., M. R. A. van Gent, D. J. R. Walstra, and A. J. H. M. Reniers (2007), Analysis of dune erosion processes in large-scale flume experiments, *Coastal Eng.*, *55*, 1028–1040.

Zijlema, M., G. Stelling, and P. Smit (2011), Swash: An operational public domain code for simulating wave fields and rapidly varied flows in coastal waters, *Coastal Eng.*, *58*, 992–1012.